IEEE Access
Multidisciplinary | Rapid Review | Open Access Journal

Date of publication xxxx 00, 0000, date of current version xxxx 00, 0000.

Digital Object Identifier ??.????/ACCESS.2021.DOI

PMSM current shaping for minimum Joule losses while reducing torque ripple and vibrations

SEBASTIAN CICEO[1,2,3], (Student member, IEEE), FABIEN CHAUVICOURT[1], JOHAN GYSELINCK[2], (Member, IEEE) and CLAUDIA MARTIS[3], (Senior member, IEEE)

[1]Engineering Consulting Services RTD, Siemens Industry Software NV, Leuven, Belgium, Email: sebastian.ciceo@siemens.com
[2]BEAMS Department, Electrical Energy Group, Université Libre de Bruxelles, Brussels, Belgium
[3]Department of Electrical Machines and Drives, Technical University of Cluj-Napoca, Cluj-Napoca, Romania

Corresponding author: Sebastian Ciceo (e-mail: sebastian.ciceo@mae.utcluj.ro).

This paper is part of the European Industrial Doctorate on Next Generation for sustaINable auTomotive ElectRical ACtuaTion (INTERACT) project which has received funding from the European Union Horizon 2020 research and innovation programme under grant agreement No 766180. Sebastian Ciceo is an Early Stage Researcher in this project. The authors also would like to acknowledge JSOL Corporation for granting access to JMAG software packages and Nicolae Zemtev from Siemens Industry Software Brasov for the help provided with the structural modeling.

ABSTRACT This paper presents a current shaping method for torque ripple and mean air-gap radial force-shape harmonics reduction, under minimum Joule losses, used for air-born and structure-born vibration reduction in 3-phase PMSM electric drives. The main source for structure-born noise in electric powertrains is the torque ripple, while the main source for air-born noise are the radial air-gap forces. The proposed method uses a Fourier-decomposed LUT model obtained from updating the 2D electromagnetic FE model using test-bench results. Modal testing is used to update the structural model, and the vibration response on the machine full RPM range is determined using the vibration-synthesis method. The proposed current shaping algorithm is deterministic and can be used on any topology of 3-phase PMSMs. The torque and mean air-gap force harmonics that are intended for reduction can be arbitrary selected and their minimization can be fully completed if the maximum current and voltage constraint are respected. On the machine under test, vibration reduction is accomplished, especially for the mechanical orders that interact with the second mode-shape.

INDEX TERMS Current shaping, MTPA, NVH, optimal control, PMSM, radial force control, torque ripple control;

I. INTRODUCTION

THE rapid advancement in automotive electrification requires higher standards for Noise and Vibration (NVH) target setting and thus development of new methods for vibration mitigation. These can be categorized as either early-design stage methods, where the design space is ample, represented by machine cross-section optimization [1], [2], or late-design stage methods where few modifications can be made. For the latter, NVH improvements can be either achieved through machine design methods [3], where small modification, such as rotor notching are made to the cross-section in order to shape the air-gap forces, or control methods where different pulse width modulation (PWM) techniques are adopted [4] or harmonic current control is performed.

On the current control side, it is possible to group by the desired minimization target: torque ripple, air-gap forces or both. Current shaping methods that minimizes the torque ripple under minimum Joule losses exists [5], while on-line, model-based torque ripple minimization strategies under Maximum-Torque-Per-Ampere (MTPA) conditions are also employed [6], by using genetic algorithms and an analytical PMSM torque ripple model for finding the optimal magnitude and phase for the 6^{th} and 12^{th} dq-current harmonics that represent the set-points to the Proportional-Resonant controllers, [7], [8] that can also include machine temperature variation [9]. In the case of Switched Reluctance Motors (SRMs) the optimal current commutation control problem is solved offline via a optimization routine for the switching-on and switching-off angles [10]. For the air-gap force control, methods based on an analytical models of the air-gap B-field

This article has been accepted for publication in a future issue of this journal, but has not been fully edited. Content may change prior to final publication. Citation information: DOI 10.1109/ACCESS.2021.3104859, IEEE Access

in function of fundamental direct/quadrature (dq) currents [11] together with FE Finite-Element (FE)-correlated analytical force models exists [12]. In [13] the authors propose a method of reducing the vibration response caused by specific radial force-shapes by using a sensitivity analysis on the 6^{th} dq-current harmonic in the electromagnetic FE simulation environment at different speed values. The resulting forces are exported to the structural-dynamics FE model for vibration computation. Optimization of different current profiles having different harmonics for air-gap force reduction is adopted in [14], while a compensation strategy for radial and tangential forces based on a measured transfer function model (harmonic currents/vibration displacement) is used in [15]. A dynamic programming optimization algorithm that relies on a saturated and rotor position-dependent FE model that minimizes the torque and radial force harmonics simultaneously by harmonic current injection is adopted in [16], while a coupled electromagnetic and structural-dynamics Permanent Magnet Synchronous Machine (PMSM) simulation tool-chain is used to achieved the same desired objective [17].

This paper proposes a new current shaping method that calculates optimal current set-points references to reduce the ripple in the torque and mean air-gap radial force (referred as DC force-shape further on) and Joule losses simultaneously. The DC-force shape harmonics reduction is important because they interact with the stator breathing mode-shape. The method works across the whole machine torque-speed envelope, leading to significant NVH improvements. It is based on Look-Up Tables (LUTs) obtained either from a pure electromagnetic FEA (Finite Element Analysis) or test-correlated FEA. The NVH benefits obtained are important because both structure-born noise caused by the torque ripple and air-born noise caused by the air-gap forces are reduced at the same time. The novelty of the method relies on the deterministic nature, the flexibility of the desired mitigated harmonics and on the fact that it can be universally applied to any PMSM having a 3-phase winding system.

The paper structure follows the diagram in Figure 1. In Section II the machine under study is presented and the procedures used to update the electromagnetic model using back-Electromotive Force (EMF) by changing the Permanent-Magnet (PM) remanence is discussed. Section III presents the harmonics LUT-based machine model (after the updating procedure is applied) that is used in Section IV, where the proposed current shaping algorithm is discussed. The effectiveness of the proposed algorithm on the vibration characteristics is tested numerically using the vibration-synthesis method [18] presented in Section V, where modal testing data is used to correlate the structural model material properties via an optimization routine. Results for the machine full speed range are presented in Section VI, where the added vibration improvements are better accounted for by using the updated structural model.

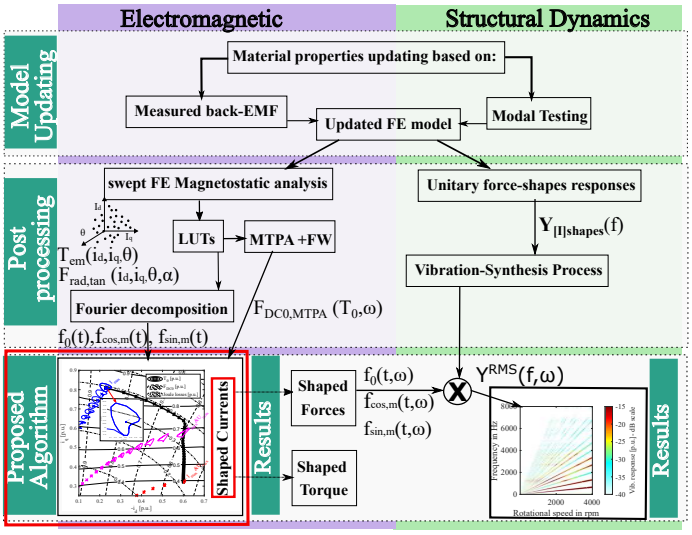

FIGURE 1. Current shaping algorithm: design and testing diagram.

II. ELECTROMAGNETIC MODEL CORRELATION USING TEST RESULTS

A. MACHINE UNDER STUDY

The machine under study is a 12/10 (12 stator teeth and 10 poles) Interior Permanent Magnet Synchronous Machine (IPMSM) with concentrated winding used in electric power steering applications with the specifications given in Table 1 and cross-section in Figure 2.

TABLE 1. IPMSM parameters

Rated power	800 W
Base speed	1650 RPM
Maximum speed	4000 RPM
Rated current	110 A (rms)
DC-link voltage	12 V
Minimum air-gap	0.5 mm
Stack length	58 mm

B. ELECTROMAGNETIC FE MODEL CORRELATION

A test-bench consisting of two identical machines coupled at the shaft (Figure 3(a)) is used to measure back-EMF in order to fit the results of the 2-Dimensional (2D) FE model. One parameter is changed in order to match the amplitude of the measured phase voltage at 1000 rpm. The PM remanent flux density (B_r) for the Neodymium-iron-boron (NdFeB) magnet material is changed using a correction factor (ΔB_r) that accounts for 3-Dimensional (3D) effects, such as PM overhang, as shown in [19]. The B-H linear curve for the PM magnetic material is modeled in the second quadrant, where $H_c' = (-B_r + \Delta B_r)/\mu_0\mu_{\text{rec}}$ is the coercive field, μ_0 is the vacuum permeability, μ_{rec} is the relative recoil permeability and $B/B_r = 1 - H/H_c'$. The slot opening (Figure 3(b)) material has the same electric steel material

This article has been accepted for publication in a future issue of this journal, but has not been fully edited. Content may change prior to final publication. Citation information: DOI 10.1109/ACCESS.2021.3104859, IEEE Access

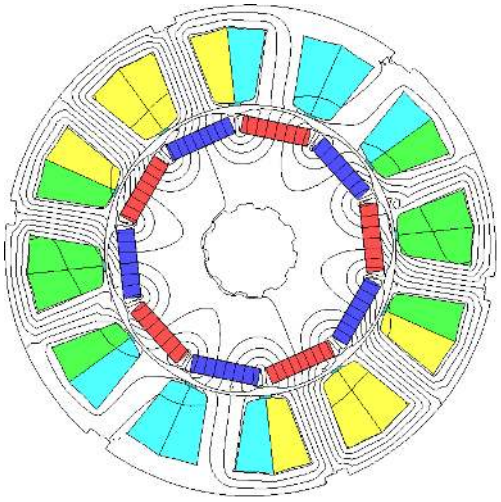

FIGURE 2. Machine cross-section with flux lines at maximum i_q current and $i_d = 0$.

(a) Electric motor test-bench.

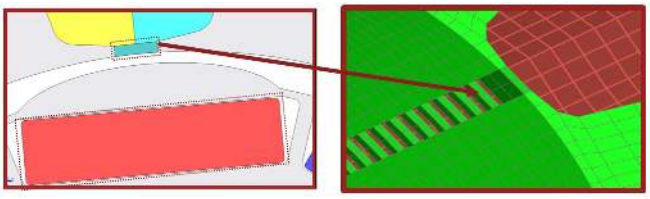

(b) 2D electromagnetic (left) and 3D strucural (right) modelling of the slot openning laminations.

FIGURE 3. PM material model updating using measured back-EMF.

properties as the stator (M800-50A), scaled down with a factor of 3 on the y-axis of the B-H curve. This accounts for the stator modular design - separated tooth segment. The back-EMF result for the correlated model is presented in Figure 4. The model updating procedure is important because the accuracy of the proposed algorithm relies on the accuracy of the electromagnetic model.

III. LOOK-UP TABLE BASED NONLINEAR PMSM MODEL

In order to simulate system-level behavior of PMSMs, high-fidelity reduced-order models [20] are needed that include saturation, cross-saturation and slotting effect. A series of magnetostatic FEA that sweep through the current (i_{dq}) and rotor position (θ_m) range are performed and the resulting electromagnetic torque (T_{em}), flux-linkages (λ_{dq}) and air-gap forces ($F_{\mathrm{rad/tan}}$) are post-processeed and stored in LUTs as shown in [21].

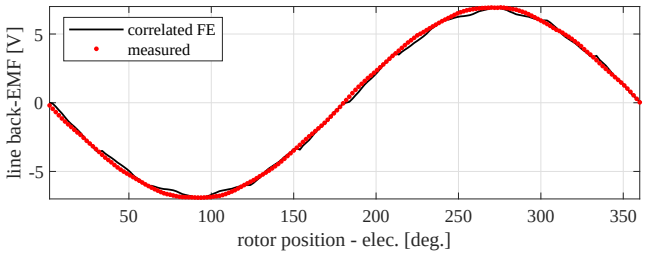

FIGURE 4. Back-EMF comparison between measured and correlated FE model at 1000 RPM.

For a 3-phase machine without homopolar current, the LUTs are either 3D with dq current and rotor position dependency (i_d, i_q, θ_e), in the case of the electromagnetic torque and flux-linkages or 4-Dimensional (4D) - adding the air-gap position dependency $(i_d, i_q, \theta_e, \alpha)$ in the case of the air-gap force, where α represents the position along the air-gap.

A. FOURIER-DECOMPOSED PMSM NONLINEAR MODEL

In order to get a better understanding of the harmonic content and reduce the size of the model, a further dimensionality reduction is applied. Specifically, the time dependency in the case of torque and air-gap force is eliminated from the LUT together with α (in the case of the force). This can be achieved by decomposing the variables stored in the LUTs into Fourier series using the cosine and sine coefficients. The variables of interest for the current shaping calculation are the electromagnetic torque (Eq. 1) - decomposed into time harmonics and the air-gap force (Eq. 2) - decomposed into space and time harmonics using the 2D Fourier transform:

$$T_{\mathrm{sup}}(t) = \sum_{n=0}^{N} T_n(t) = T_0(t) + \sum_{n=1}^{N} (T_{\mathrm{cos,n}} \cdot \cos(nt) + T_{\mathrm{sin,n}} \cdot \sin(nt)) \text{ and} \tag{1}$$

$$F_{\mathrm{sup}}(t, \alpha) = \sum_{m=0}^{M} F_m(t, \alpha) = F_{\mathrm{DC}}(t) + \sum_{m=1}^{M} (F_{\mathrm{cos,n}}(t) \cdot \cos(m\alpha) + F_{\mathrm{sin,n}}(t) \cdot \sin(m\alpha)), \tag{2}$$

where T_{sup} is the superposed torque waveform that includes all time-dependent harmonic amplitude factors (T_0, $T_{\mathrm{sin,n}}$, $T_{\mathrm{cos,n}}$) until the maximum truncated N order and F_{sup} is the 2D superposed air-gap force-wave that contains all space-dependent harmonic amplitude factors (F_{DC} and $F_{\mathrm{sin,n}}, F_{\mathrm{con,n}}$) up to order M.

Additionally, the resulting DC force-shape (F_{DC}) is again decomposed into time-dependent harmonic amplitude factors ($F_{\mathrm{DC,0}}$, $F_{\mathrm{DCsin,n}}$, $F_{\mathrm{DCcos,n}}$) as in the torque case (Eq. 3), where F_{DCsup} is the superposed DC force-shape that contains all factors up to order N:

This article has been accepted for publication in a future issue of this journal, but has not been fully edited. Content may change prior to final publication. Citation information: DOI 10.1109/ACCESS.2021.3104859, IEEE Access

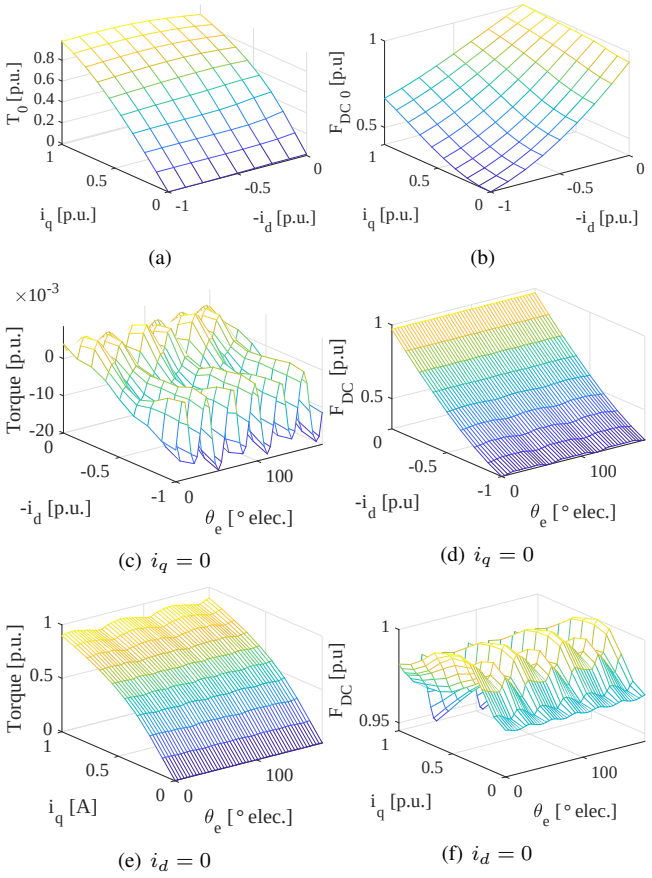

FIGURE 5. Torque and DC force-shape position current and position dependency.

$$F_{\mathrm{DCsup}}(t) = \sum_{n=0}^{N} F_{\mathrm{DC,n}}(t) = F_{\mathrm{DC0}}(t) + \sum_{n=1}^{P} (F_{\mathrm{DCcos,n}} \cdot \cos(nt) + F_{\mathrm{DCsin,n}} \cdot \sin(nt)), \tag{3}$$

Figure 5 shows the torque and radial DC force-shape dependency measured in per-unit (p.u.) system, where the base unit represents the maximum value of each quantity with respect to i_d, i_q (again, measured in p.u.) and the electrical rotor position θ_e. It can be noticed that higher torque ripple appear in the flux-weakening region (after the base speed) while higher force ripple appear in the maximum torque region.

A further reduction in the model size is achieved by truncating the harmonic content of the torque (Eq. 4) and DC force-shape (Eq. 5) wave by using the most significant harmonics in the dq frame, in this case the 0, 6^{th} and 12^{th} dq-frame harmonics, as shown (the time dependency is replaced with θ_e):

$$T_{\mathrm{em}}(i_d, i_q, \theta_e) = T_0(i_d, i_q) + T_{\mathrm{ripple}}(i_d, i_q, \theta_e) = T_0(i_d, i_q) + T_{\cos 6}(i_d, i_q)\cos(6\theta_e) + T_{\sin 6}(i_d, i_q)\sin(6\theta_e) + + T_{\cos 12}(i_d, i_q)\cos(12\theta_e) + T_{\sin 12}(i_d, i_q)\sin(12\,\theta_e), \tag{4}$$

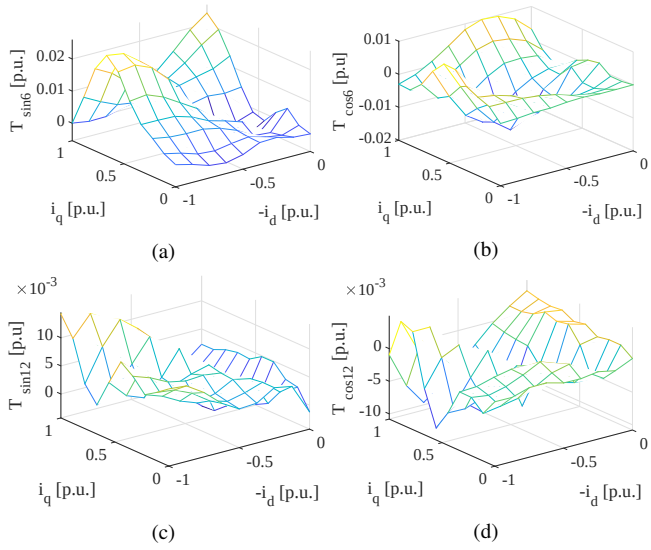

FIGURE 6. Torque harmonic factors: 6^{th} (a-b) and 12^{th} (c-d).

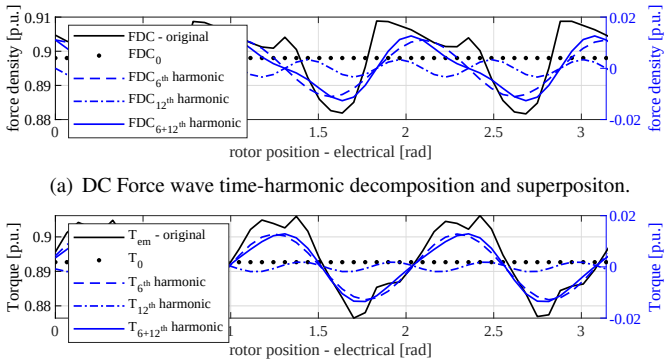

FIGURE 7. Dimensionality reduction via Fourier decomposition for $i_d = 0.25$ p.u. and $i_d = 0.89$ p.u.

$$F_{\mathrm{DC}}(i_d, i_q, \theta_e) = F_{\mathrm{DC0}}(i_d, i_q) + F_{\mathrm{DCripple}}(i_d, i_q, \theta_e) = F_{\mathrm{DC0}}(i_d, i_q) + F_{\mathrm{DCcos6}}(i_d, i_q)\cos(6\theta_e) + + F_{\mathrm{DCsin6}}(i_d, i_q)\sin(6\theta_e) + F_{\mathrm{DCcos12}}(i_d, i_q)\cos(12\theta_e) + + F_{\mathrm{DCsin12}}(i_d, i_q)\sin(12\theta_e), \tag{5}$$

where the i_{dq} dependent torque Fourier $\cos - \sin$ orthogonal basis are presented in Figure 6.

The waveform results of the torque and radial DC force-shape for one specific operating point is shown in Figure 7.

IV. OPTIMAL CURRENT SHAPING FOR TORQUE AND DC FORCE-SHAPE RIPPLE CONTROL

In order to minimize the torque and force ripple, the i_{dq} current must be shaped in such a way that it contains counteracting harmonics to the original ripple. The set-points for the mean torque (T_0^*), mean component of the DC force-shape (F_{DC0}^*) and given fixed rotor position (θ_e^*) are considered

This article has been accepted for publication in a future issue of this journal, but has not been fully edited. Content may change prior to final publication. Citation information: DOI 10.1109/ACCESS.2021.3104859, IEEE Access

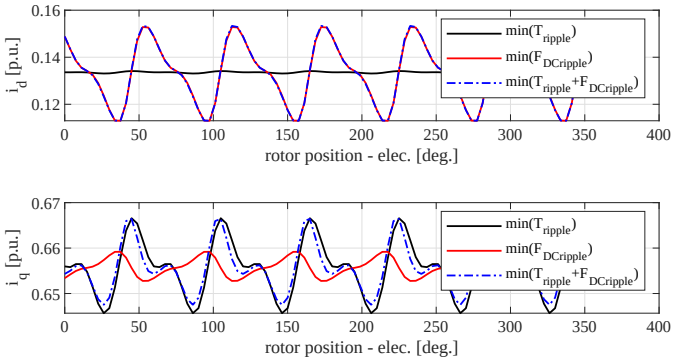

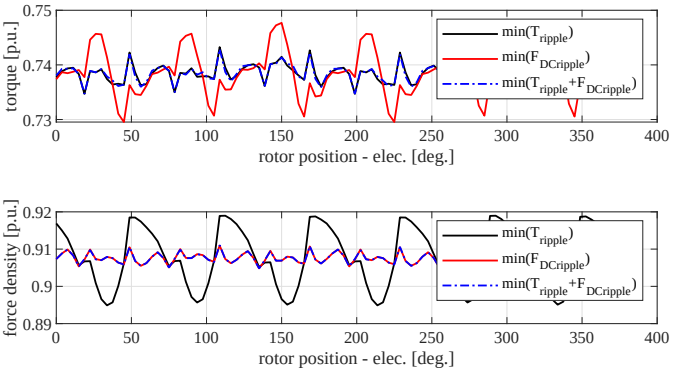

FIGURE 8. Shaped currents for different ripple minimization goals for $T_0^* = 0.738$ [p.u] and $F_{\mathrm{DC0}}^* = 0.907$ [p.u.].

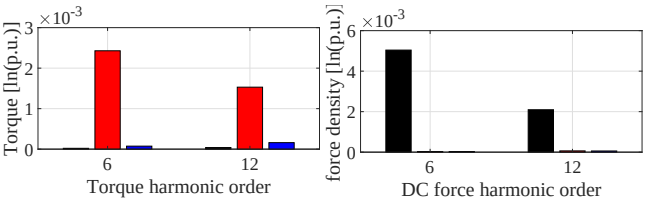

FIGURE 9. Resulting torque and DC force-shape for different ripple minimization goals using the shaped currents showed in Figure 8.

input to the problem and the optimal currents represent the output. This can be formulated as a system of non-linear equations that are solved for i_d and i_q:

$$\begin{cases} T_0(i_d, i_q) - T_0^* + T_{\mathrm{ripple}}(i_d, i_q, \theta_e^*) = 0 \\ F_{\mathrm{DC0}}(i_d, i_q) - F_{\mathrm{DC0}}^* + F_{\mathrm{ripple}}(i_d, i_q, \theta_e^*) = 0. \end{cases} \tag{6}$$

By solving two equations for each set of dq currents (i_d, i_q) at each rotor position (θ_e^*), the solution is fully determined for a specific set of $(T_0^*, F_{\mathrm{DC0}}^*, \theta_e^*)$. Eq. (6) has the objective of minimizing the torque ripple (T_{ripple}) and radial DC force-shape ripple (F_{DCripple}) concurrently. If the torque ripple is omitted from the formulation, the solution minimizes the DC force ripple only and, vice-versa, if the DC force ripple is omitted the solution minimizes the torque ripple only. Figure 8 shows the harmonic shaped currents for the 3 different optimization scenarios, with the magnitude and phase of the introduced current harmonics resulting from Eq.(6). In this paper only the harmonics shown in Eq.(4) and Eq.(5) are used because the 6^{th} and 12^{th} harmonics are the main contributors to the torque and mean air-gap force ripple. Also, the extension of the algorithm to higher order harmonics, such as the 18^{th} and 24^{th}, would require a higher controller bandwidth in practice, which may lead to implementation issues. It can be noticed that the difference in the wave-shape is caused by the difference in the 6^{th} and 12^{th} current harmonic amplitude, while the DC component remains the same. Figure 9 shows that torque and radial DC force ripple are not fully eliminated because of the existence of higher harmonics that are originally truncated in the problem statement.

In order to shape the currents on the full torque-speed range, including the flux-weakening (FW) region, for each operating condition (each desired torque set-point and speed), a MTPA optimization is performed where the degrees of freedom (DOF) are again (i_d, i_q) and the resulting mean component of the DC force-shape is stored for each torque and speed set-point $(F_{\mathrm{DC0,MTPA}}(T_0^*, \omega_e^*))$:

$$\begin{cases} \text{minimize Joule losses: } R_s(i_d^2 + i_q^2) \\ \text{equality constraint: } T_0(i_d, i_q) - T_0^* = 0 \\ \text{current limit: } \sqrt{(i_d^2 + i_q^2)} \le I_{\max} \\ \text{voltage limit: } \sqrt{u_d(i_d, i_q, \omega_e^*)^2 + u_q(i_d, i_q, \omega_e^*)^2} \le U_{\max}, \end{cases} \tag{7}$$

where R_s is the phase resistance, $I_{\max}$ and $U_{\max}$ are the maximum current and voltage values given by the power electronics module, and u_d, u_q are the dq phase voltages.

By including the mean component of the DC force-shape obtained from solving the optimization problem $(F_{\mathrm{DC0,MTPA}}(T_0^*, \omega_e^*))$ in Eq.(6), a new system of equations is formed that solves for the dq currents at each rotor position, speed and each mean torque reference:

$$\begin{cases} T_0(i_d, i_q, \omega_e^*) - T_0^* + T_{\mathrm{ripple}}(i_d, i_q, \theta_e^*, \omega_e^*) = 0 \\ F_{\mathrm{DC0}}(i_d, i_q, \omega_e^*) - F_{\mathrm{DC0,MTPA}}(T_0^*, \omega_e^*) + \\ F_{\mathrm{DCripple}}(i_d, i_q, \theta_e^*, \omega_e^*) = 0. \end{cases} \tag{8}$$

The results from solving this equation set are DC torque, speed and rotor position-dependent set of currents $i_{\mathrm{dq}}(T_0, \omega_e, \theta_e)$. T_0, F_{DC0} and the Joule losses are mapped in Figure 10 on the i_{dq} range together with the (i_d, i_q) current loci for maximum T_0 at different speed values (where the p.u. system for the losses is constructed using as base unit the maximum value in the i_{dq} range). It can be remarked that maximum T_0 value is decreasing with the increase in speed after the base speed is reached.

This approach leads to having the same Root-Mean-Square (RMS) Joule losses as in the case of the MTPA control strategy as exemplified in Figure 11. It can be remarked that different i_{dq} orbits obtained from the current shaping

This article has been accepted for publication in a future issue of this journal, but has not been fully edited. Content may change prior to final publication. Citation information: DOI 10.1109/ACCESS.2021.3104859, IEEE Access

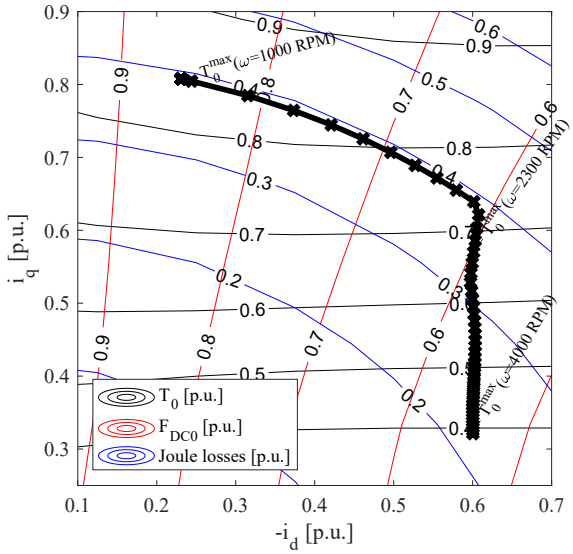

FIGURE 10. Contour plot for T_0, F_{DC0} and Joule losses on the i_{dq} plane.

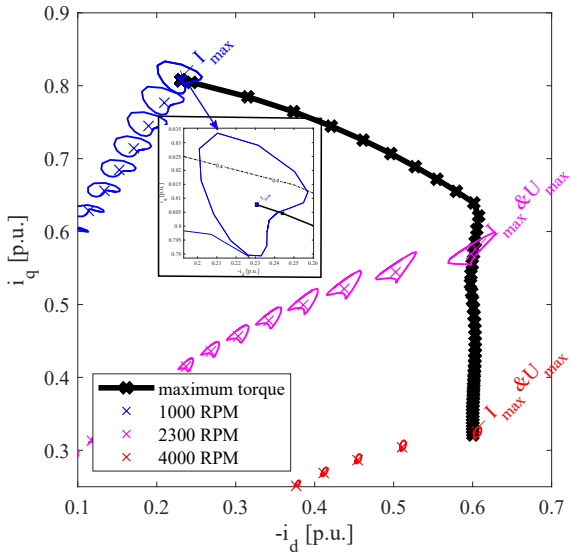

FIGURE 11. Set of (i_d, i_q) current loci for the proposed current shaping algorithm (marked with a solid line) and standard MTPA (marked with crosses) for different speed and torque values and maximum T_0 at different speed values (marked with black crosses).

algorithm are formed for different reference mean torque and speed values, centered around the value obtained from the MTPA (with flux-weakening) optimization problem.

In order to determine the maximum envelope of the torque-speed map, the mean torque is set to be the maximum value for the given speed $i_{\mathrm{dq}}^{T_0^{\max}}$ $(T_0 = T_0^{\max}(\omega_e, \theta_e))$. These currents are shown in Figure 12 representing the i_{dq} speed and rotor position dependent envelope where for each speed, a harmonic current range that center around the values obtained

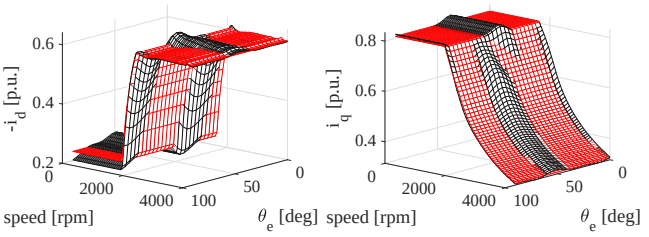

FIGURE 12. Harmonic-shaped (black) and constant (red) dq current values for maximum mean torque across the speed range.

from the standard MTPA (with flux-weakening) is formed. Until the base speed of 1650 RPM the maximum current is the only valid constraint, whereas in the flux-weakening region the voltage limit takes effect.

V. VIBRATION RESPONSE FOR THE FULL TORQUE-RPM RANGE USING THE VIBRATION-SYNTHESIS METHOD

A. STRUCTURAL FE MODEL CORRELATION

Experimental Modal Analysis (EMA) is performed on the machine (with the rotor removed) in order to determine the modal parameters: natural frequencies, mode shapes and modal damping. The test output is the measured output/input Frequency Response Functions (FRF) - $H_{o/i}$ in free-free boundary conditions. A miniature shaker (LMS Qsource SN045) is used to excite the structure and 36 evenly-distributed triaxial (3D) accelerometers (PCB Piezotronics SN 356A22) placed on the housing's outer surface are used to measure the vibration response. Simcenter SCADAS Lab is used for the data acquisition and the PolyMAX algorithm [22] is used to determine the modal parameters: modal damping ζ_k, residuals A_k and natural frequencies ω_k for each mode k until the maximum truncated mode n, in the desired frequency range (up to 5000Hz) of the linear modal model (where * is the complex conjugate):

$$H_{o/i}(\omega) = \sum_{k=1}^{n} \frac{A_k}{j\omega - \lambda_k} + \frac{A_k^*}{j\omega - \lambda_k^*}, \quad \text{with } \lambda_k = -\zeta_k\omega_k + j\sqrt{1-\zeta_k^2}\omega_k \,. \tag{9}$$

Using the extracted modal parameters, the anisotropic material properties of the structural FE model (Youngs modulus, shear modulus and the Poisson ratio) are updated in order to match the test results using a optimization routine with the modal frequency difference and the Modal Assurance Criterion (MAC) as correlation metrics [23].

Results from the optimization procedure are presented in Figure 14, where the (a,b) subplots show the deflection for the in-plane ovalization (2,0) and triangle (3,0) mode-shapes obtained with the PolyMax algorithm. The 3D accelerometers placement can also be remarked in the mentioned figures. In the (c,d) subplots the updated FE mode-shapes are shown. It can be noticed that by updating the material properties

This article has been accepted for publication in a future issue of this journal, but has not been fully edited. Content may change prior to final publication. Citation information: DOI 10.1109/ACCESS.2021.3104859, IEEE Access

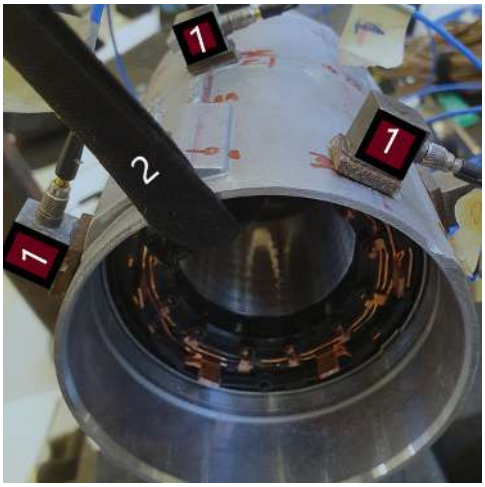

FIGURE 13. EMA test setup where the electric motor with the removed rotor is kept in free-free boundary conditions by the elastic bungee cord (marked with the label 2) and the 3D accelerometers (highlighted in red and marked with label 1) used to measure vibration.

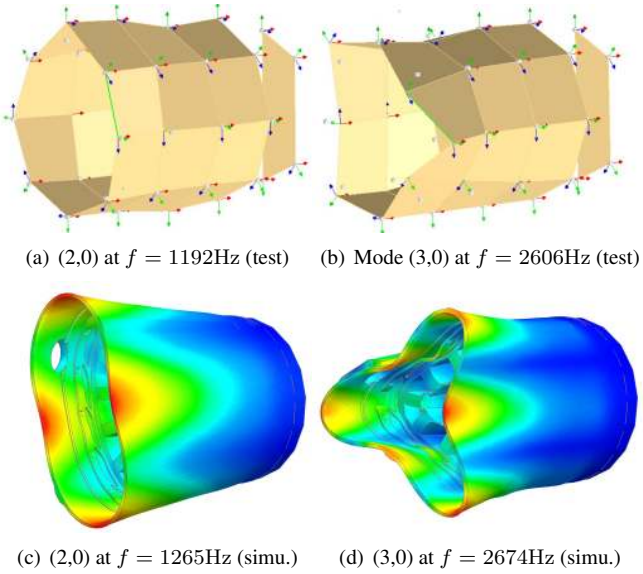

(a) (2,0) at $f = 1192$Hz (test) (b) Mode (3,0) at $f = 2606$Hz (test)

(c) (2,0) at $f = 1265$Hz (simu.) (d) (3,0) at $f = 2674$Hz (simu.)

FIGURE 14. Machine operational deflection shapes (a,b) and correlated FE modal results (c,d).

a relative frequency error below 5% is obtained for each test/simulation mode-shape pair.

B. SPATIALLY DECOMPOSED AIR-GAP FORCE

The link between electromagnetic and structural physics computation domain is the radial and tangential air-gap force densities computed using the Maxwell Stress Tensor. $i_{\mathrm{dq}}^{T_0^{\max}}$ is used to interpolate the air-gap B-fields LUTs ($B_{\mathrm{rad,tan}}(i_d, i_q, \theta_m, \alpha)$) obtained in Section III:

$$\begin{aligned} &F_{\mathrm{rad}}(\omega_e, t, \alpha) = \\ &\frac{1}{2\mu_0}\left(B_{\mathrm{rad}}^2(i_{\mathrm{dq}}^{T_0^{\max}}(\theta_e, \omega_e), \alpha) - B_{\mathrm{tan}}^2(i_{\mathrm{dq}}^{T_0^{\max}}(\theta_e, \omega_e), \alpha)\right) \\ &F_{\mathrm{tan}}(\omega_e, t, \alpha) = \\ &\frac{1}{\mu_0} B_{\mathrm{rad}}\left(i_{\mathrm{dq}}^{T_0^{\max}}(\theta_e, \omega_e), \alpha\right) B_{\mathrm{tan}}\left(i_{\mathrm{dq}}^{T_0^{\max}}(\theta_e, \omega_e), \alpha\right). \end{aligned} \tag{10}$$

The force is expressed as spatially decomposed superposition of the most important excitation shapes using the $\cos - \sin$ orthogonal basis according to Eq. (2) for each value of the speed, resulting in time and speed dependent amplitude factors $f_{\mathrm{DC}}(\omega_e, t)$, $f_{\mathrm{cos,m}}(\omega_e, t)$ and $f_{\mathrm{sin,m}}(\omega_e, t)$ for the maximum torque envelope.

The vibration is calculated as the superposition of dynamic responses excited by each significant force-shape. This is achieved with a modal frequency response solution, having the excitation $F_{[I],\mathrm{shape}}$ a unitary force-shape:

$$v_{[I],\mathrm{shape}}^i(\omega_e, f) = H^i(f) F_{[I],\mathrm{shape}}(\omega_e, f), \tag{11}$$

where $v_{[I],\mathrm{shape}}^i(\omega_e, f)$ is the frequency response in node i for each force-shape excitation, with $H^i(f)$ the output obtained from modal analysis. The total response in node i - $v^i(\omega_e, f)$ is the superposition of all frequency responses scaled with the cos-sin frequency domain amplitude factors:

$$\begin{aligned} &v^i(\omega_e, f) = v_{[I],\mathrm{DC}}^i(f) f_{DC}(\omega_e, f) + \\ &+ \sum_{m=1}^{M} \left(v_{[I],\mathrm{cos,m}}^i f_{\mathrm{cos,m}}(\omega_e, f) + v_{[I],\mathrm{sin,m}}^i f_{\mathrm{sin,m}}(\omega_e, f)\right), \end{aligned} \tag{12}$$

where the RMS response for all N nodes is:

$$v^{RMS}(\omega_e, f) = \sqrt{\frac{1}{N}\sum_{i=1}^{N} v^i(\omega_e, f)^2}. \tag{13}$$

The structural mesh is shown in Figure 15 where 6 output nodes are selected in order to compute the RMS vibration response.

VI. RESULTS

A. TORQUE AND FORCE

Run-up results for the maximum torque and corresponding DC force-shape over the full RPM range are presented in Figure 16. Two results sets , one with the standard MTPA (with flux-weakening) control strategy, and one with the proposed algorithm are shown. It can be observed that both in the case of the torque and DC force-shape the mechanical orders $f = 30 f_{mech}$ and $f = 60 f_{\mathrm{mech}}$ (f_{mech} is the base mechanical frequency) caused by the 6^{th} and 12^{th} dq-current harmonics are completely reduced, with order-cuts shown in Figure 17.

B. VIBRATION RESPONSE

The vibration response is computed using the method described in Section V. The first result set shown in Figure

This article has been accepted for publication in a future issue of this journal, but has not been fully edited. Content may change prior to final publication. Citation information: DOI 10.1109/ACCESS.2021.3104859, IEEE Access

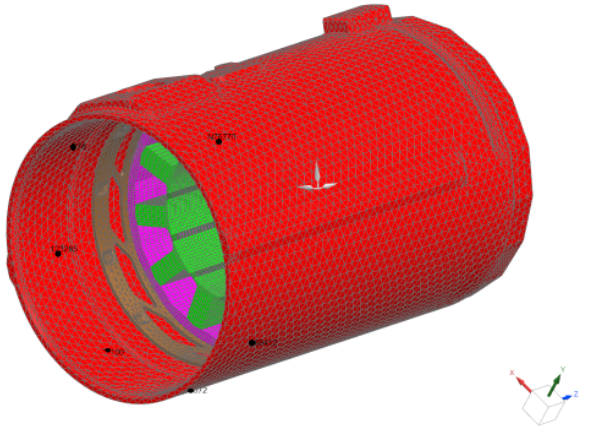

FIGURE 15. Structural mesh with the output vibration computation nodes present on the housing marked in black.

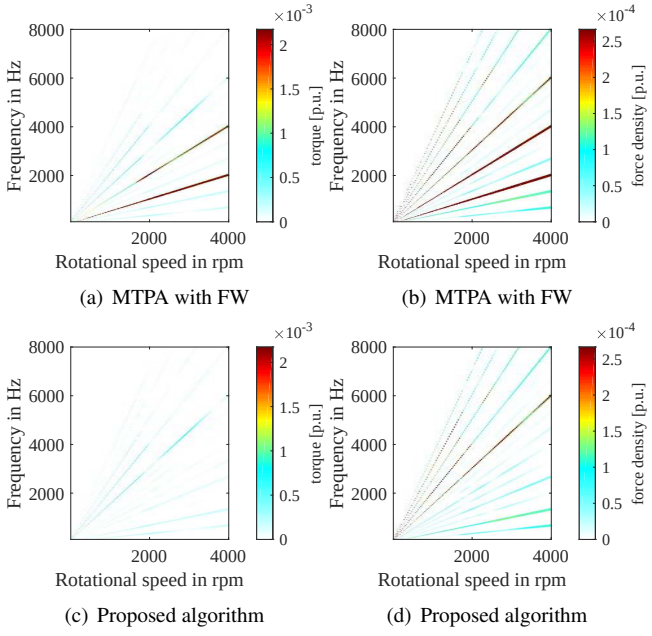

FIGURE 16. Torque and DC force-shape run-up results.

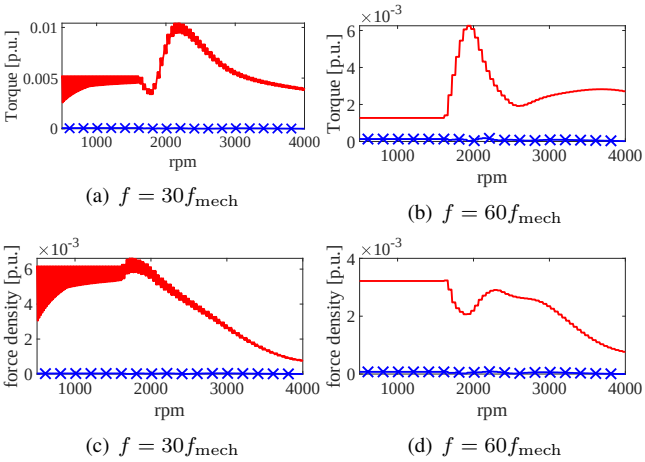

FIGURE 17. Torque and DC force-shape order-cuts for the standard MTPA with flux-weakening (red) and proposed algorithm (blue, with markers): (a,c) - 30^{th} order and (b,d) - 60^{th} order.

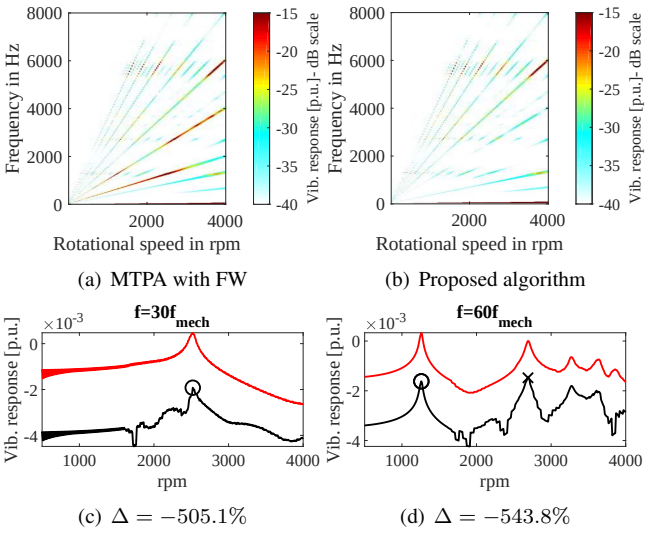

FIGURE 18. Scaled run-up vibration response spectogram (a,b) and order-cuts ((c) - 6^{th} order and (d) - 60^{th} order) using only the DC force-shape, where the MTPA (with flux-weakening) results are represented in (red) and proposed algorithm in (black) and the peak caused by the resonance effect of mode (2,0) is marked with a circle symbol and mode (3,0) with a cross symbol.

18 represents the vibration displacement for the full RPM-frequency range using just the radial DC force-shape as structural loading ($v_{\mathrm{DC}}^{\mathrm{RMS}}(\omega_e, f)$). This procedure is done in order to compare the effect that the proposed algorithm versus the standard MTPA (with flux-weakening) strategy has on the vibration response. Figure 18 (c,d) represents the mechanical order-cuts and show a significant decrease of order 30 and 60 when using the proposed algorithm, where the relative change in amplitude peak response between the proposed algorithm and the standard MTPA (with flux-weakening) control uses the Δ symbol.

The second result set shown in Figure 19 represents again the vibration displacement for the full RPM-frequency using a number of 40 force-shapes (from the 0 to 40) as structural loading ($v^{\mathrm{RMS}}(\omega_e, f)$). The upper-bound for the force-shape spatial harmonics (40) is limited by Nyquist criterion with the number of nodes along the circumference of the structural mesh. Again, the procedure is adopted for control algorithm comparison and to determine the total effect of radial DC force-shape harmonics reduction on the structural response.

Figure 19 (c,d) represents the mechanical order-cuts for the case where all force-shapes are used to excite the structure, with the first two orders (8 and 10) sorted in terms of the highest vibration peak shown. The first 10 mechanical orders are quantified in Table 2 in terms of amplitude peak (measured in $10^{-3}p.u.$) and relative peak change Δ. It is observable that the proposed algorithm is beneficial for decreasing 3 out of 4 orders in terms of peak: 40^{th}, 50^{th} and 70^{th}, where the 20^{th} order represents the exception.

Because the method can be universally applied to 3-phase

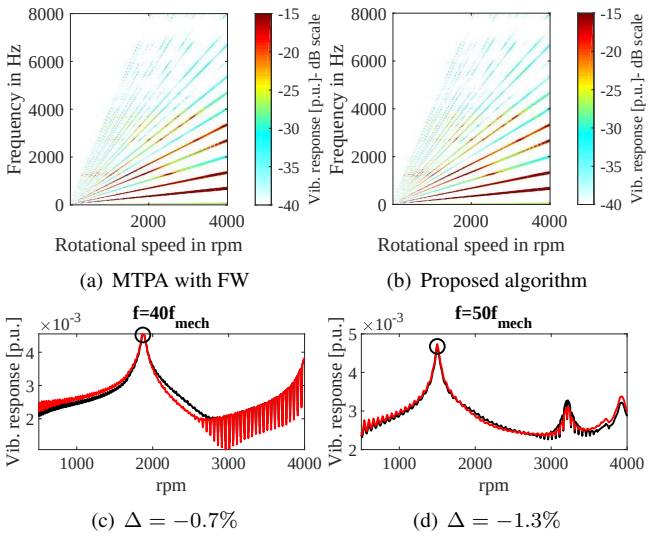

FIGURE 19. Scaled run-up vibration response spectogram (a,b) and order-cuts with the highest vibration-displacement ((c) - 40^{th} order and (d) - 50^{th} order) using all force-shapes, where the MTPA (with flux-weakening) results are represented in (red) and proposed algorithm in (black), where the peak caused by the resonance effect of mode (2,0) is marked with a circle symbol.

TABLE 2. Run-up order-cuts peaks

f	$10f_{mech}$	$20f_{mech}$	$30f_{mech}$	$40f_{mech}$	$50f_{mech}$
peak	47	43	34	45	47
Δ	0%	+2.54%	+1.5%	-0.72%	-1.29%
f	$60f_{mech}$	$70f_{mech}$	$80f_{mech}$	$90f_{mech}$	$100f_{mech}$
peak	24	40	37	21	35
Δ	-8%	-1.38%	+20%	+4.03%	+13.24%

PMSMs it is reasonable to assume that more significant decrease in vibration response caused by the minimization of DC force-shape harmonics will occur in the case of traction motors. This is explained in [24] where the breathing mode-shape (mode 0) that is excited by harmonics caused by the DC force-shape represents the main source of NVH issues in traction machines.

VII. CONCLUSIONS

In this paper, a novel current shaping method used in 3-phase PMSMs that reduces the torque and mean radial air-gap force harmonics under MTPA conditions is proposed. The method relies on solving a system of nonlinear equations and uses experimentally-updated Fourier-decomposed LUT models for the machine torque and air-gap force. The method efficiency for PMSM NVH characteristics is validated using a experimentally-updated structural model via the vibration-synthesis. It shows results both in terms of torque ripple reduction, which is the main contributor for the machine structure-born noise, and air-born vibration reduction during run-up operation. If the maximum current and voltage limitation allows, the targeted harmonics in both the torque and mean radial air-gap force can be completely reduced. The consequence of force reduction on the machine vibration characteristics at maximum torque across the whole speed range is a decrease in vibration peaks on the main mechanical orders of 0.72% for the 40^{th} order and 1.29% for the 50^{th} order.

As a further investigation, the additional iron losses caused by the harmonic currents should be investigated. Also, the harmonic current injection will be implemented on the test-bench where the practical implementation of harmonic control algorithm, model uncertainty and micro-controller computational speed have to be taken into consideration.

REFERENCES

[1] A.-C. Pop, J. J. Gyselinck, D. E. Pinto, and I. Vintiloiu, "Optimization of low-power brushless PM-machines for automotive applications with focus on high-volume mass production," *IEEE Transactions on Industrial Electronics*, vol. 64, no. 12, pp. 9767–9775, 2017.

[2] I. Ibrahim, R. Silva, M. Mohammadi, V. Ghorbanian, and D. A. Lowther, "Surrogate-based acoustic noise prediction of electric motors," *IEEE Transactions on Magnetics*, vol. 56, no. 2, pp. 1–4, 2020.

[3] S. Ciceo, F. Chauvicourt, B. Varaticeanu, J. Gyselinck, and C. Martis, "PMASynRM late design-stage rotor shape NVH optimization," in *2020 International Conference on Electrical Machines (ICEM)*, vol. 1. IEEE, 2020, pp. 278–283.

[4] A. Ruiz-Gonzalez, M. J. Meco-Gutierrez, F. Perez-Hidalgo, F. Vargas-Merino, and J. R. Heredia-Larrubia, "Reducing acoustic noise radiated by inverter-fed induction motors controlled by a new PWM strategy," *IEEE Transactions on Industrial Electronics*, vol. 57, no. 1, pp. 228–236, 2009.

[5] G. Bramerdorfer, W. Amrhein, S. M. Winkler, and M. Affenzeller, "Identification of a nonlinear pmsm model using symbolic regression and its application to current optimization scenarios," in *IECON 2014-40th Annual Conference of the IEEE Industrial Electronics Society*. IEEE, 2014, pp. 628–633.

[6] S. Decker, M. Brodatzki, B. Bachowsky, B. Schmitz-Rode, A. Liske, M. Braun, and M. Hiller, "Predictive trajectory control with online MTPA calculation and minimization of the inner torque ripple for permanent-magnet synchronous machines," *Energies*, vol. 13, no. 20, p. 5327, 2020.

[7] C. Lai, G. Feng, K. L. V. Iyer, K. Mukherjee, and N. C. Kar, "Genetic algorithm-based current optimization for torque ripple reduction of interior PMSMs," *IEEE Transactions on Industry Applications*, vol. 53, no. 5, pp. 4493–4503, 2017.

[8] C. Lai, G. Feng, K. Mukherjee, V. Loukanov, and N. C. Kar, "Torque ripple minimization for interior PMSM with consideration of magnetic saturation incorporating online parameter identification," *IEEE Transactions on Magnetics*, vol. 53, no. 6, pp. 1–4, 2017.

[9] C. Lai, G. Feng, K. Mukherjee, and N. C. Kar, "Investigations of the influence of PMSM parameter variations in optimal stator current design for torque ripple minimization," *IEEE Transactions on Energy Conversion*, vol. 32, no. 3, pp. 1052–1062, 2017.

[10] J. Deskur, T. Pajchrowski, and K. Zawirski, "Optimal control of current switching angles for high-speed SRM drive," *COMPEL-The international journal for computation and mathematics in electrical and electronic engineering*, 2010.

[11] M. Kanematsu, T. Miyajima, H. Fujimoto, Y. Hori, T. Enomoto, M. Kondou, H. Komiya, K. Yoshimoto, and T. Miyakawa, "Suppression control of radial force vibration due to fundamental permanent-magnet flux in IPMSM," in *2013 IEEE Energy Conversion Congress and Exposition*. IEEE, 2013, pp. 2821–2826.

[12] T. Hara, S. Aoyagi, T. Ajima, Y. Iwaji, and R. Yoshizu, "Proposal of vibration control reducing 2nd radial electromagnetic force," *Electrical Engineering in Japan*, vol. 198, no. 1, pp. 45–53, 2017.

[13] M. Watahiki, T. Mori, L. Lan, J. Tanaka, T. Ueda, T. Fukumura, M. Kanematsu, and H. Fujimoto, "Reduction of sixth-order radial force by harmonic current control and its application to EPS motors," *Electrical Engineering in Japan*, vol. 209, no. 3-4, pp. 45–56, 2019.

[14] J. Krotsch and B. Piepenbreier, "Radial forces in external rotor permanent magnet synchronous motors with non-overlapping windings," *IEEE Transactions on Industrial Electronics*, vol. 59, no. 5, pp. 2267–2276, 2011.

[15] J. Andresen, S. Vip, A. Mertens, and S. Paulus, "Compensation of the radial and circumferential mode 0 vibration of a permanent magnet electric machine based on an experimental characterisation," in *2020 22nd European Conference on Power Electronics and Applications (EPE'20 ECCE Europe)*. IEEE, 2020, pp. P–1.

[16] M. Harries, M. Hensgens, and R. W. De Doncker, "Noise reduction via harmonic current injection for concentrated-winding permanent magnet synchronous machines," in *2018 21st International Conference on Electrical Machines and Systems (ICEMS)*. IEEE, 2018, pp. 1157–1162.

[17] J. Nägelkrämer, A. Heitmann, and N. Parspour, "Application of dynamic programming for active noise reduction of PMSM by reducing torque ripple and radial force harmonics," in *2018 AEIT International Annual Conference*. IEEE, 2018, pp. 1–6.

[18] M. Boesing, T. Schoenen, K. A. Kasper, and R. W. De Doncker, "Vibration synthesis for electrical machines based on force response superposition," *IEEE Transactions on Magnetics*, vol. 46, no. 8, pp. 2986–2989, 2010.

[19] D.-K. Woo, D.-K. Lim, H.-K. Yeo, J.-S. Ro, and H.-K. Jung, "A 2-D finite-element analysis for a permanent magnet synchronous motor taking an overhang effect into consideration," *IEEE Transactions on Magnetics*, vol. 49, no. 8, pp. 4894–4899, 2013.

[20] M. Tahkola, J. Keränen, D. Sedov, M. F. Far, and J. Kortelainen, "Surrogate modeling of electrical machine torque using artificial neural networks," *IEEE Access*, vol. 8, pp. 220 027–220 045, 2020.

[21] S. Ciceo, F. Chauvicourt, J. Gyselinck, and C. Martis, "A comparative study of system-level PMSM models with either current or flux-linkage state variables used for vibro-acoustic computation," in *2019 IEEE International Electric Machines & Drives Conference (IEMDC)*. IEEE, 2019, pp. 1881–1888.

[22] B. Peeters, H. Van der Auweraer, P. Guillaume, and J. Leuridan, "The polyMAX frequency-domain method: a new standard for modal parameter estimation?" *Shock and Vibration*, vol. 11, no. 3, 4, pp. 395–409, 2004.

[23] F. Chauvicourt, C. Faria, J. Gyselinck, and W. Desmet, "Validation of homogenization technique used for accurate predictions of laminated structures mechanical behavior," in *Proceedings of ISMA2016 International Conference on Noise and Vibration Engineering*. KU Leuven, 2016, pp. 1–8.

[24] A. Hofmann, F. Qi, T. Lange, and R. De Doncker, "The breathing mode-shape 0: Is it the main acoustic issue in the PMSMs of today's electric vehicles?" in *2014 17th International Conference on Electrical Machines and Systems (ICEMS)*. IEEE, 2014, pp. 3067–3073.

SEBASTIAN CICEO obtained his M.Sc in Electrical Engineering from the Technical University of Cluj-Napoca in 2017. He currently works at Siemens PLM Software, Leuven as an Early-stage researcher (ESR) in the frame of the H2020 MSCA EID 2017-2021 research project INTERACT. He is pursuing a joint PhD degree with Université Libre de Bruxelles and the Technical University of Cluj-Napoca. He's main research interest are: model-based system engineering and testing, electrical machines and drives, electrical mobility, structural dynamics, multibody dynamics, multi-physics optimization and control and data-driven engineering.

FABIEN CHAUVICOURT received his M.Sc. degree (2014) in Mechanical Engineering from the Université de Technologie de Compiégne, and his double PhD degree (2018) in Mechanical Engineering from the Katholieke Universiteit Leuven, Belgium and in Electrical Engineering from Université Libre de Bruxelles, Belgium. He is currently a Research Engineer within Siemens Industry Software NV focusing his research on model-based engineering (electric powertrain development, multi-physical system-level modelling, virtual integration of component behavior) and data-driven engineering (artificial intelligence, machine learning, signal processing).

JOHAN GYSELINCK obtained his M.Sc. and PhD degree in electromechanical engineering at the Ghent University (Belgium) in 1991 and 2000 respectively. From 2000 till 2004 he was post-doctoral researcher and lecturer at the University of Liége (Belgium). Since 2004 he is professor at the Université Libre de Bruxelles (ULB, Belgium). His main teaching and research topics are low-frequency numerical magnetics, electrical machines and drives, and renewables (wind and photovoltaics). He is (co-)author of some 270 journal and conference papers.

CLAUDIA MARTIS was born in 1967 in Macin, Romania. She started her university studies in 1985 at the Polytechnic Institute in Cluj-Napoca and she graduated Electrical Engineering in 1990. After three years working as engineer at SINTEROM SA Cluj-Napoca, she joined the Chair of Electrical Machines, Marketing and Management, at the Technical University of Cluj-Napoca, first as associated assistant and, since 1996, as full-time teaching and research assistant. In 1994 she enrolled also as PhD student at the same Chair, under the coordination of professor Karoly-Agoston Biro. She graduated in 2001 after the public defense of the PhD thesis entitled: "Contributions to the study of doubly-salient permanent magnet reluctance machines". Currently she is full professor at the Department of Electrical Machines and Drives, Faculty of Electrical Engineering, Technical University of Cluj-Napoca.